Customizing oxygen electrocatalytic microenvironment with S, N codoped carbon nanofibers confining carbon nanocapsules and Co$_9$S$_8$ nanoparticles for rechargeable Zn-air batteries

Chen Yang [a], Jie Chen [a], Lei Yan [b],[*],[1], Yijing Gao [c],[*],[1], Jiqiang Ning [d], Yong Hu [a],[b],[**],[1]

[a] *Key Laboratory of the Ministry of Education for Advanced Catalysis Materials, Department of Chemistry, Zhejiang Normal University, Jinhua 321004, China*
[b] *College of Chemistry and Materials Engineering, Zhejiang A&F University, Hangzhou 311300, China*
[c] *Zhejiang Engineering Laboratory for Green Syntheses and Applications of Fluorine-Containing Specialty Chemicals, Institute of Advanced Fluorine-Containing Materials, Zhejiang Normal University, Jinhua 321004, China*
[d] *Department of Optical Science and Engineering, Fudan University, Shanghai 200438, China*

A R T I C L E   I N F O

A B S T R A C T

Rational design and modulation of oxygen electrocatalytic microenvironment are crucial for achieving high performance in rechargeable Zn-air batteries (RZABs). We report a high-efficiency bifunctional electrocatalyst based on S, N codoped carbon fibers confining carbon nanocapsules attached with Co$_9$S$_8$ nanoparticles to customize the oxygen electrocatalytic microenvironment. The inner carbon nanocapsules function as a "gas buffer", while the outer fiber skeleton acts as a self-supporting structure, which jointly refine the oxygen electrocatalytic microenvironment and improve accessibility of the active sites. Such a unique nanostructure proves advantageous for O$_2$ adsorption/diffusion and mitigation of local pH changes during oxygen reduction reaction, and favors the release of generated O$_2$ and the transfer of interfacial electron during the oxygen evolution reaction as well. The constructed liquid RZABs deliver a large peak power density (280 mW cm^{-2}) and robust cyclability (1200 h at 10 mA cm^{-2}), and the assembled quasi-solid state flexible RZABs further indicate long-term durability.

1. Introduction

The increasing global demand for energy and the severe environmental pollution resulting from overreliance on fossil fuels have prompted substantial exploration of energy conversion and storage systems, including water splitting devices, fuel cells and metal-air batteries [1–3]. Among them, rechargeable zinc-air batteries (RZABs) have gained special prominence due to their high safety, low-cost and impressive theoretical energy density (1086 Wh kg$_{Zn}^{-1}$), making them one of ideal devices for energy storage and conversion [4–6]. Currently, the primary challenge impeding the widespread adoption of RZABs is the sluggish kinetics of the oxygen evolution reaction (OER) and oxygen reduction reaction (ORR) at the air cathode [7]. These electrocatalytic reactions significantly influence the discharge and charge performance of RZAB, ultimately determining energy efficiency and cycle life [8].

Consequently, developing highly efficient bifunctional electrocatalysts for ORR and OER is of utmost importance in addressing the bottleneck and advancing the field of rechargeable metal-air batteries.

In recent years, researchers have predominantly attained commendable bifunctional electrochemical performance by identifying suitable catalysts and systematically regulating active sites [9–11]. Various materials, such as heteroatom-doped carbon, transition metal compounds and perovskite oxides [12–15], along with strategic methodologies including Mott-Schottky heterostructure construction, defect engineering and heteroatom doping [16–18], have been employed to enhance the intrinsic electrocatalytic activities. Nevertheless, despite continuous enhancements in the bifunctional electrocatalytic activities of reported materials, the performance of RZABs assembled with them has displayed unsatisfactory behavior [19–21]. This phenomenon can be easily attributed to fact that the operating environment of cathode

---

catalysts within assembled batteries diverges from those experienced in half-cell tests. Specifically, the electrocatalytic process of cathode catalysts in RZABs takes place at gas-solid-liquid three-phase interfaces and operates under ambient atmosphere conditions without the need for additional O_2 supply. In contrast, the rotating disk electrode (RDE) technique, frequently employed in three-electrode systems, necessitates a specific rotation rate, an oxygen-saturated electrolyte. These distinctions underscore the sensitivity of the catalytic sites to the local microenvironment under battery operating environment, such as the reactant/intermediate species concentration [22], interfacial electron transfer [23], the diffusion of reactants and products [24], local pH [25], and some other factors. The term microenvironment is defined as the region extending from the catalyst surface to a few micrometers away, where the diffusion and distribution of reaction species are major determinants of reaction kinetics and mass transport [26]. For instance, Liu and his colleagues proposed the assembly of hydrophobic fluorinated covalent organic framework (COF) nanosheets onto FeNi layered-double-hydroxide (FeNi LDH) [27], which function as aerophilic "nano-islands" to enlarge the area of three-phase boundaries and enhance O_2 mass transfer. The RZAB employing COF-modified air cathode exhibits significantly improved energy efficiency and enhanced cycle durability compared to traditional FeNi LDH cathode. Therefore, integration of the intrinsic activity of catalysts with a suitable local microenvironment is an intelligent strategy for optimizing the required catalytic reaction to achieve efficient performance of RZABs.

Indeed, the morphology of the catalyst can significantly influence the local microenvironment and intrinsic activity of the active sites. Numerous studies have demonstrated that the pore structure and three-dimensional architecture of the materials play a crucial role in the diffusion of gas and electrolyte, impacting the formation and stability of the three-phase interface, and closely modulating the reaction kinetics of OER/ORR [28,29]. For instance, under high local O_2 concentration and accelerated OH^- diffusion, the active sites will promote the reduction of O_2 via the dominant 4-electron pathway [30,31]. Additionally, the intrinsic activity of active sites can be modulated by regulating the morphology of carrier material through strong electronic metal-support interactions. The introduction of nanopores or curvature in the carbon matrix induces changes in the position and local coordination configuration of the metal sites [32,33]. For example, $Fe-N_4$ sites in a helical carbon substrate with high-curvature surface induce compressive strain on the Fe-N bonds, resulting in a lowered ORR energy barrier [34]. Consequently, rationally designing the nanostructure of the oxygen electrocatalyst is expected to achieve efficient catalytic reaction by concurrently optimizing the microenvironment and promoting intrinsic activity. However, there is currently a paucity of in-depth research on the impact of different morphologies on the microenvironment, particularly the absence of experimental proof from the perspective of mass transport at the catalyst interface.

Motivated by the above considerations, we propose an optimization of the microenvironment of the oxygen electrocatalyst through structural engineering to fulfill the requirements of high-performance and stable RZABs. For this purpose, an optimized bifunctional electrocatalyst, composed of carbon nanocapsules attached with Co_9S_8 nanoparticles (NPs) and wrapped in S, N codoped carbon fibers (denoted as $CNC/Co_9S_8@SNCF$) was designed and synthesized. Comparative analysis with other structures underscores that such a multilayer macroporous fiber architecture can tailor the local environment of electrocatalyst (Scheme 1), which shows stronger mass transport capabilities at the reaction interface and enables the supported Co_9S_8 NPs to exhibit superior OER/ORR intrinsic activity. Experiments and finite element method (FEM) simulations confirm that the regulating morphology benefits the increase in O_2 concentration and reduces the local pH change during the ORR process, and promotes the rapid release of the generated O_2 and contact with the electrolyte/electrode interface during the OER process. Density functional theory (DFT) reveals that the presence of nanocapsules in the fibers optimizes the adsorption energy of Co_9S_8 sites for intermediates, thereby reducing catalytic barriers and improving selectivity. As a result, the $CNC/Co_9S_8@SNCF$ catalyst exhibits excellent pH-universal ORR catalytic activity and OER performance. Impressively, the $CNC/Co_9S_8@SNCF$-based liquid RZABs yields substantial power density (280 mW cm^{-2}), high specific capacity (758 mAh g^{-1}) and favorable stability performance (1200 h at 10 mA cm^{-2}). The assembled sandwich-shaped and fiber-shaped flexible RZABs also offer good power density, long-term durability and versatility in various applications.

2. Experimental

2.1. Materials

Cobalt(II) acetate tetrahydrate (Co(CH$_3$COO)$_2$·4 H$_2$O, ≥99%), tetraethyl orthosilicate (TEOS, AR), ammonia (AR), 3-Hydroxytyramine hydrochloride (AR), thiourea (AR), N, N-Dimethylformamide (DMF, AR), polyacrylonitrile (PAN, M$_w$ 150,000), potassium hydroxide (KOH, AR), absolute ethanol (AR), and Nafion solution (5.0 wt%, in lower aliphatic alcohols and water). All the chemicals were purchased from Sinopharm Chemical Reagent Co., Ltd. (China) and directly used without further purification. Deionized water was used throughout the work.
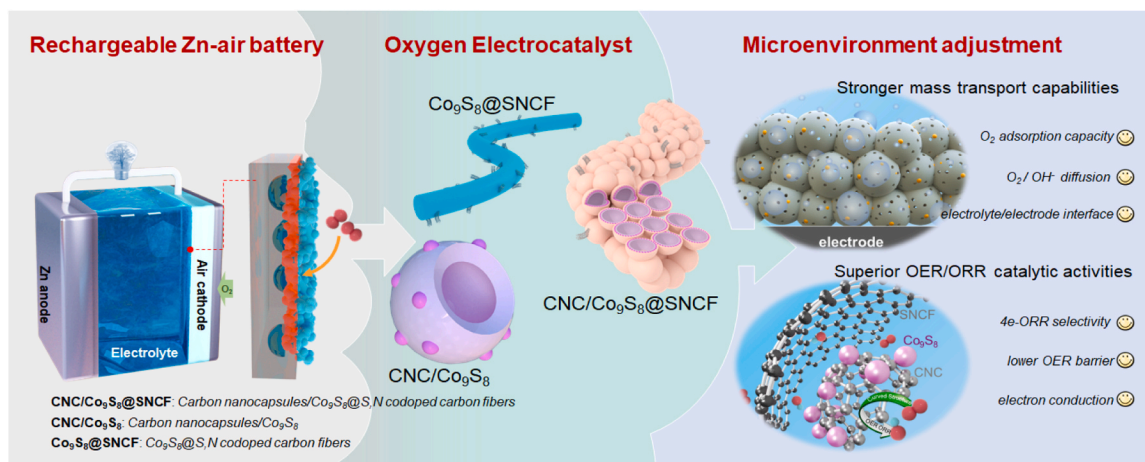
Scheme 1. Schematic illustration of structural engineering of oxygen electrocatalyst on the interface microenvironment and battery performance.

2.2. Preparation of SiO$_2$@PDA nanospheres

In a typical synthesis, 24 mL of absolute ethanol and 80 mL of water were combined in a beaker under magnetic stirring for 10 minutes at room temperature. Subsequently, 1 mL of aqueous ammonia was added dropwise and stirred for an additional 10 minutes. Following this, 1 mL of TEOS was introduced to the mixture and stirred for another 10 minutes. Afterward, 400 mg 3-Hydroxytyramine hydrochloride, dissolved in 8 mL water, was added to the above solution. The resulting brown solution was centrifuged, washed several times with DI water, and dried in the oven at 60 °C overnight to obtain SiO$_2$@PDA nanospheres.

2.3. Preparation of SiO$_2$@PDA/Co^{2+}@PAN fibers

The electrospinning solution was prepared by dissolving 0.4 g of PAN, 1 g SiO$_2$@PDA and 0.25 g Co(CH$_3$COO)$_2$ in 5.0 mL of DMF through vigorous stirring overnight. The mixture was then transferred to a 5 mL plastic syringe with a 22-gauge tip needle for the electrospinning. The applied potential, solution flow rate, and spinning distance were 15 kV, 1 mL h^{-1}, and 18 cm, respectively. Aluminum foil was used as a collector with a rotating speed of 10 rpm. After spinning, the resulting SiO$_2$@PDA/Co^{2+}@PAN fibers were dried at 60 °C for 24 hours.

2.4. Preparation of CNC/Co$_9$S$_8$@SNCF

The SiO$_2$@PDA/Co^{2+}@PAN fibers were first stabilized at 260 °C for 1 h with a heating rate of 2 °C min^{-1} under air atmosphere. Subsequently, the obtained fibers were vulcanized with a certain amount of thiourea (10 times the mass of fibers) at 900 °C for 3 h at a heating rate of 5 °C min^{-1} under N$_2$ atmosphere. Finally, the flexible fiber film CNC/Co$_9$S$_8$@SNCF was obtained by subjecting it to a 4 M KOH etching process for 10 h at room temperature to remove the SiO$_2$ template.

2.5. Preparation of Co$_9$S$_8$@SNCF

The synthesis procedure of Co$_9$S$_8$@SNCF was similar to that of CNC/Co$_9$S$_8$@SNCF except for the absence of SiO$_2$@PDA in the electrospinning solution.

2.6. Preparation of CNC@Co$_9$S$_8$

For the preparation of CNC@Co$_9$S$_8$, a solution of 1 g SiO$_2$@PDA and 0.25 g Co(CH$_3$COO)$_2$ in 5.0 mL of DMF was vigorously stirred overnight, followed by centrifugation to obtain SiO$_2$@PDA/Co^{2+} precursor. Then, the SiO$_2$@PDA/Co^{2+} precursor was vulcanized with a certain amount of thiourea (10 times the precursor mass) at 900 oC for 3 h with a heating rate of 5 °C min^{-1} under N$_2$ atmosphere. Finally, the CNC@Co$_9$S$_8$ sample was prepared by 4 M KOH alkaline etching treatment for 10 h at room temperature.

2.7. Preparation of pure Co$_9$S$_8$ and CNC@SNCF samples

0.25 g Co(CH$_3$COO)$_2$ vulcanized with 2.5 g thiourea at 900 oC for 3 h with a heating rate of 5 °C min^{-1} under N$_2$ atmosphere to prepare pure Co$_9$S$_8$ sample. The synthesis procedure of CNC@SNCF was similar to that of CNC/Co$_9$S$_8$@SNCF except for the absence of Co(CH$_3$COO)$_2$ in the electrospinning solution.

Other experimental details including material characterizations, electrochemical ORR and OER measurements, assembly of liquid and flexible Zn-air battery experiments, O$_2$ diffusivity in catalyst layer, and theoretical calculations can be found in the Appendix A. Supplementary data.

3. Results and discussion

3.1. Composition and microstructure of CNC/Co$_9$S$_8$@SNCF

The synthesis procedure for CNC/Co$_9$S$_8$@SNCF is illustrated in Fig. 1a. Initially, SiO$_2$@polydopamine (SiO$_2$@PDA) nanospheres were prepared through a one-pot method that involved the hydrolysis of tetraethoxysilane and the polymerization of dopamine hydrochloride. The scanning electron microscopy (SEM) analysis reveals the homogeneous size of SiO$_2$@PDA nanospheres, with an average diameter of 400 nm (Fig. S1). Subsequently, SiO$_2$@PDA, in conjunction with metal ions (Co^{2+}), was electrospun with PAN to produce SiO$_2$@PDA/Co^{2+}@PAN fibers. The surface of SiO$_2$@PDA nanospheres exhibits a negative zeta potential of −39.4 eV due to the presence of catechol and amine functional groups (Fig. S2), facilitating the facile physical adsorption of Co^{2+}. Through the electrospinning process, the derived SiO$_2$@PDA/Co^{2+}@PAN fibers form an interconnected network of continuous fibers, and the SiO$_2$ nanospheres create a densely packed architecture along the long axis of fibers (Fig. S3). The synthesis of CNC/Co$_9$S$_8$@SNCF involved high-temperature sulfurization of SiO$_2$@PDA/Co^{2+}@PAN, followed by alkaline etching treatment. Throughout these processes, the inner hollow PDA layer and the outer PAN layer were carbonized to create carbon frameworks. Simultaneously, the adsorbed Co ions were transformed into Co$_9$S$_8$ NPs, which catalyzed the formation of carbon nanotubes (CNTs) [35,36].

The SEM image of CNC/Co$_9$S$_8$@SNCF (Fig. 1b) illustrates carbon fibers with uneven surfaces interconnected to form three-dimensional carbon frameworks. The high-resolution SEM image (Fig. 1c) reveals that fiber surfaces are dominantly covered with regularly sized hollow carbon nanocapsules, alongside self-catalytically generated CNTs. Further characterization of CNC/Co$_9$S$_8$@SNCF using transmission electron microscopy (TEM) indicated that the internal structures consist of hollow carbon nanocapsules with spherical void spaces of approximately 380 nm, corresponding to the SiO$_2$@PDA template (Fig. 1d). These nanocapsules feature curved nanoshells with a thickness of about 20 nm (Fig. 1e), interconnected through PAN-derived carbon, and accompanied by the presence of CNTs growing outside the carbon shell (Fig. S4). This interconnected hollow structure is expected to facilitate efficient gas and ion transport, thus enhancing the reaction kinetics. High-resolution TEM (HRTEM) of the selected regions (Fig. 1f) unveils the highly crystalline structure of Co$_9$S$_8$, with the interplanar crystal distance of 0.30 nm corresponding to (311) crystal planar. This multiple carbon protection of PAN-derived carbon in the outer layer and carbon nanocapsules inner shell ensures the stability of Co$_9$S$_8$ NPs in the highly alkaline electrolyte. Selected area electron diffraction (SAED) pattern (Fig. 1g) exhibits two apparent rings attributable to the (311) and (440) crystal planes of Co$_9$S$_8$. Additionally, X-ray diffraction (XRD) analysis (Fig. 1h) confirms the crystalline structures of CNC/Co$_9$S$_8$@SNCF, with characteristic diffraction peaks of Co$_9$S$_8$ (JCPDS No. 19–0364), consistent with the HRTEM results. Energy dispersive X-ray analysis (EDX) mappings (Fig. S5) indicate the coexistence and dispersion of Co, S, N and C elements within the fibers. For comparative purposes, control samples, Co$_9$S$_8$@SNCF and CNC/Co$_9$S$_8$, were synthesized with crystalline phase structures similar to CNC/Co$_9$S$_8$@SNCF, but with distinct morphologies (Figs. S6 and S7). Specifically, the former reveals the configuration of simple carbon fibers, whereas the latter exhibits hollow carbon spheres.

X-ray photoelectron spectroscopy (XPS) analysis was performed to examine the elemental composition of CNC/Co$_9$S$_8$@SNCF, as well as two control samples. The survey spectrum reveals characteristic peaks corresponding to Co, S, N and C elements (Fig. S8 and Table S1). High-resolution Co 2p spectra, depicted in Fig. 1i, can be deconvoluted into three doublets representing the Co-S bond (778.6 and 793.6 eV), Co^{3+} (780.4 and 795.4 eV) and Co^{2+} (782.2 and 797.2 eV), accompanied by two satellite peaks [37]. Notably, the binding energies of the Co 2p spectrum in CNC/Co$_9$S$_8$@SNCF are similar to those of CNC/Co$_9$S$_8$, but

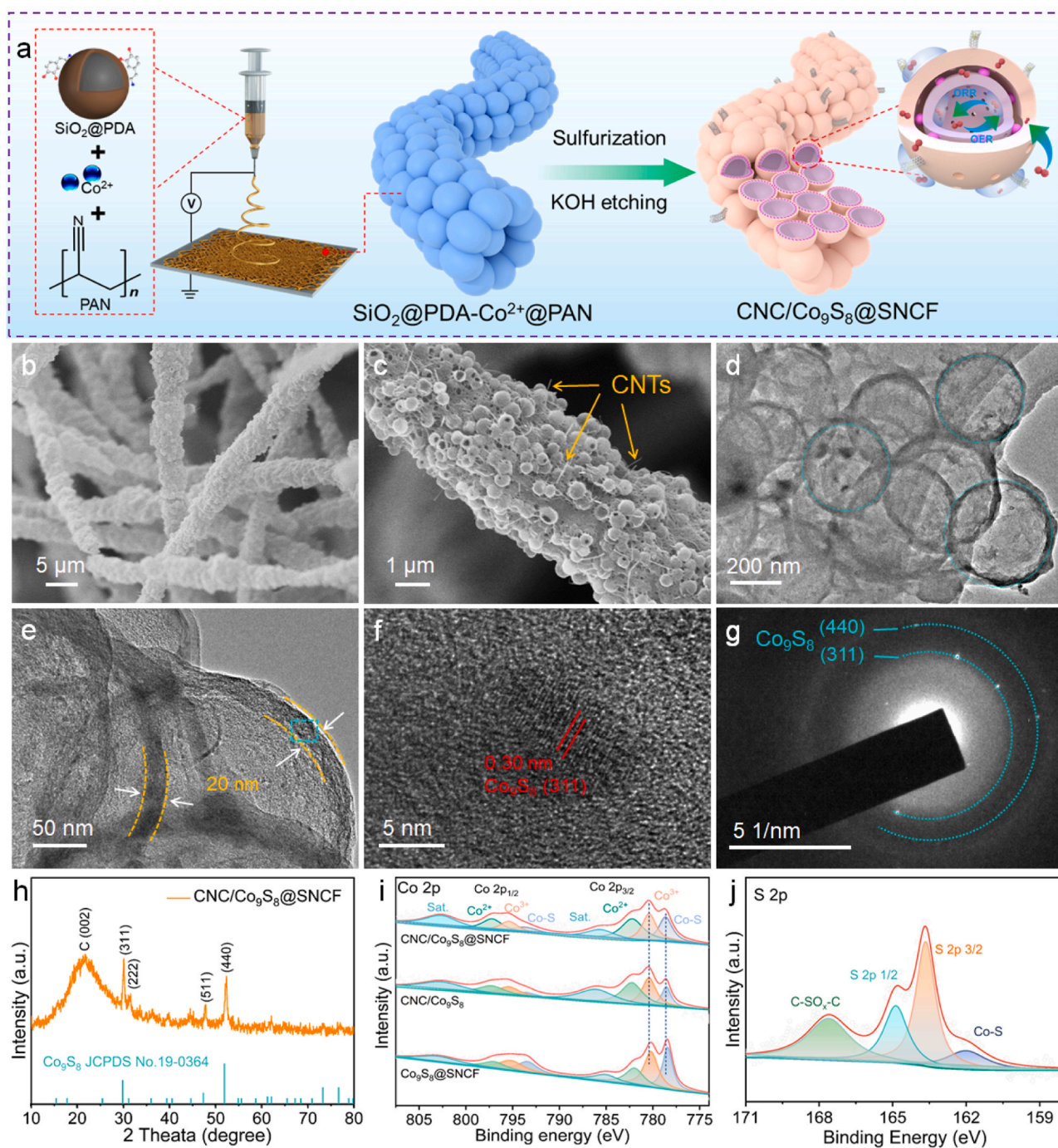**Fig. 1.** (a) Synthetic procedure, (b, c) SEM images, (d, e) TEM images, (f) HRTEM image, (g) SAED pattern and (h) XRD pattern of the CNC/Co$_9$S$_8$@SNCF. (i) High-resolution Co 2p XPS spectra of the CNC/Co$_9$S$_8$@SNCF, CNC/Co$_9$S$_8$ and Co$_9$S$_8$@SNCF. (j) S 2p of CNC/Co$_9$S$_8$@SNCF.

significantly higher than those of Co$_9$S$_8$@SNCF, implying that the carbon nanocapsules may affect the electronic state of Co. According to reports, the electronic structure of metals can be affected by the electronic metal-support interacting [38], so for these embedded Co$_9$S$_8$ NPs, their electronic structure might be intimately associated with the microenvironment provided by the carbon nanocapsule. High-resolution N 1 s spectrum (Fig. S9) identifies four nitrogen species: pyridinic N (398.2 eV), Co-N$_x$ (399.2 eV), pyrrolic N (400.8 eV) and graphitic N (402.1 eV) [39,40]. The presence of Co-N$_x$ species suggests the interaction between Co$_9$S$_8$ NPs and N-doped carbon layers, which is believed to reduce the energy barrier and enhance the OER/ORR activities [41,42]. In S 2p XPS spectrum (Figs. 1j and S10), the peak at

162.0 eV is attributed to Co-S bond in Co$_9$S$_8$. The peaks at 163.7 and 164.9 eV are related to the sulfur atoms incorporated into the carbon framework (C-S-C), and the peaks at 167.6 eV are attributed to the oxidation state of sulfur (C-SO$_x$-C) [43,44]. XPS etching experiments (Fig. S11) provide further evidence that S is located in both the inner carbon nanocapsule as well as the outer fiber skeleton.

3.2. Electrocatalytic performance towards ORR and OER

To evaluate the bifunctional catalytic performance of the prepared catalysts, the ORR activities are first investigated by using RDE at 1600 rpm in a 0.1 M KOH electrolyte. Commercial Pt/C (20 wt%) was

selected as the benchmark ORR catalyst. As demonstrated in Fig. S12, cyclic voltammetry (CV) curve for CNC/Co$_9$S$_8$@SNCF shows a prominent peak in the O$_2$-saturated KOH solution, while featureless in the N$_2$-saturated electrolyte, indicating the occurrence of oxygen reduction. Linear sweep voltammetry (LSV) curves (Fig. 2a) further reveal that the most positive half-wave potential (E$_{1/2}$) for CNC/Co$_9$S$_8$@SNCF is 0.87 V (vs. RHE), surpassing the values for CNC/Co$_9$S$_8$ (0.84 V), Co$_9$S$_8$@SNCF (0.82 V) and Pt/C (0.85 V) catalysts (Table S2). Additionally, the Tafel slope for CNC/Co$_9$S$_8$@SNCF is 73 mV dec^{-1} (Fig. 2b), demonstrating superior reaction kinetics compared to CNC/Co$_9$S$_8$ (75 mV dec^{-1}) and Co$_9$S$_8$@SNCF (80 mV dec^{-1}). The CNC/Co$_9$S$_8$@SNCF catalyst exhibits a kinetic current density (J$_k$) of 10.6 mA cm^{-2} at 0.85 V in 0.1 M KOH solution, approximately two times that of commercial Pt/C (4.5 mA cm^{-2}). Fig. 2c and Table S3 illustrate comparative performance diagrams for CNC/Co$_9$S$_8$@SNCF with other reported catalysts, clearly highlighting that it exhibits significantly better ORR activity in alkaline media. As shown in the Koutecky-Levich (K-L) plots derived from rotating disk measurements at different rotation speeds (Fig. S13), a consistent slope allows for good linearity at different potentials, reflecting the first-order kinetics of the ORR process. Selectivity and stability are crucial parameters for evaluating catalytic performance. The rotating ring disk electrode (RRDE) technique was conducted to assess the ORR selectivity. As illustrated in Fig. S14, the electron transfer number (n) of CNC/Co$_9$S$_8$@SNCF is about 4.0, with H$_2$O$_2$ yields below 5%, confirming its superior four-electron selectivity pathway for ORR compared with CNC/Co$_9$S$_8$ and Co$_9$S$_8$@SNCF. The durability of CNC/

Co$_9$S$_8$@SNCF was investigated by the chronoamperometric tests (Fig. S15), revealing that the current density can be maintained at about 93%, significantly higher than commercial Pt/C (46%). Besides, CNC/Co$_9$S$_8$@SNCF exhibits better methanol tolerance compared to Pt/C (Fig. S16), when methanol is introduced into electrolyte during the ORR process.

The CNC/Co$_9$S$_8$@SNCF catalyst also exhibits commendable ORR performance in both acidic and neutral environments. Notably, it displays E$_{1/2}$ values of 0.73 V in 0.5 M H$_2$SO$_4$ and 0.74 V in 0.1 M PBS (Figs. 2d and S17a), comparable to those of the commercial Pt/C (0.75 V and 0.68 V, respectively). Additionally, the CNC/Co$_9$S$_8$@SNCF catalyst possesses the lowest Tafel slopes of 95 mV dec^{-1} and 92 mV dec^{-1} in acidic and neutral media, respectively (Figs. 2e and S17b), in contrast to control samples. Furthermore, the CNC/Co$_9$S$_8$@SNCF catalyst achieves a considerable J$_k$ of 4.3 mA cm^{-2} at 0.7 V in acidic media, inferior to the commercial Pt/C (9.9 mA cm^{-2}). In 0.1 M PBS, it attains a J$_k$ of 12.5 mA cm^{-2} at 0.6 V, surpassing the commercial Pt/C (11.7 mA cm^{-2}). The excellent ORR kinetics of CNC/Co$_9$S$_8$@SNCF under different pH conditions may be attributed to its interconnected hollow fiber structure with large porosity, which facilitates the exposure of more internal active sites and accelerates mass transfer. The CNC/Co$_9$S$_8$@SNCF catalyst shows relatively attractive ORR performance in neutral and acidic solutions, respectively, outperforming most reported materials (Figs. 2f and S17c). A comparative analysis with other pH-universal catalysts, as detailed in Tables S4 and S5, underscores significant potential of the CNC/Co$_9$S$_8$@SNCF catalyst for applications in pH-
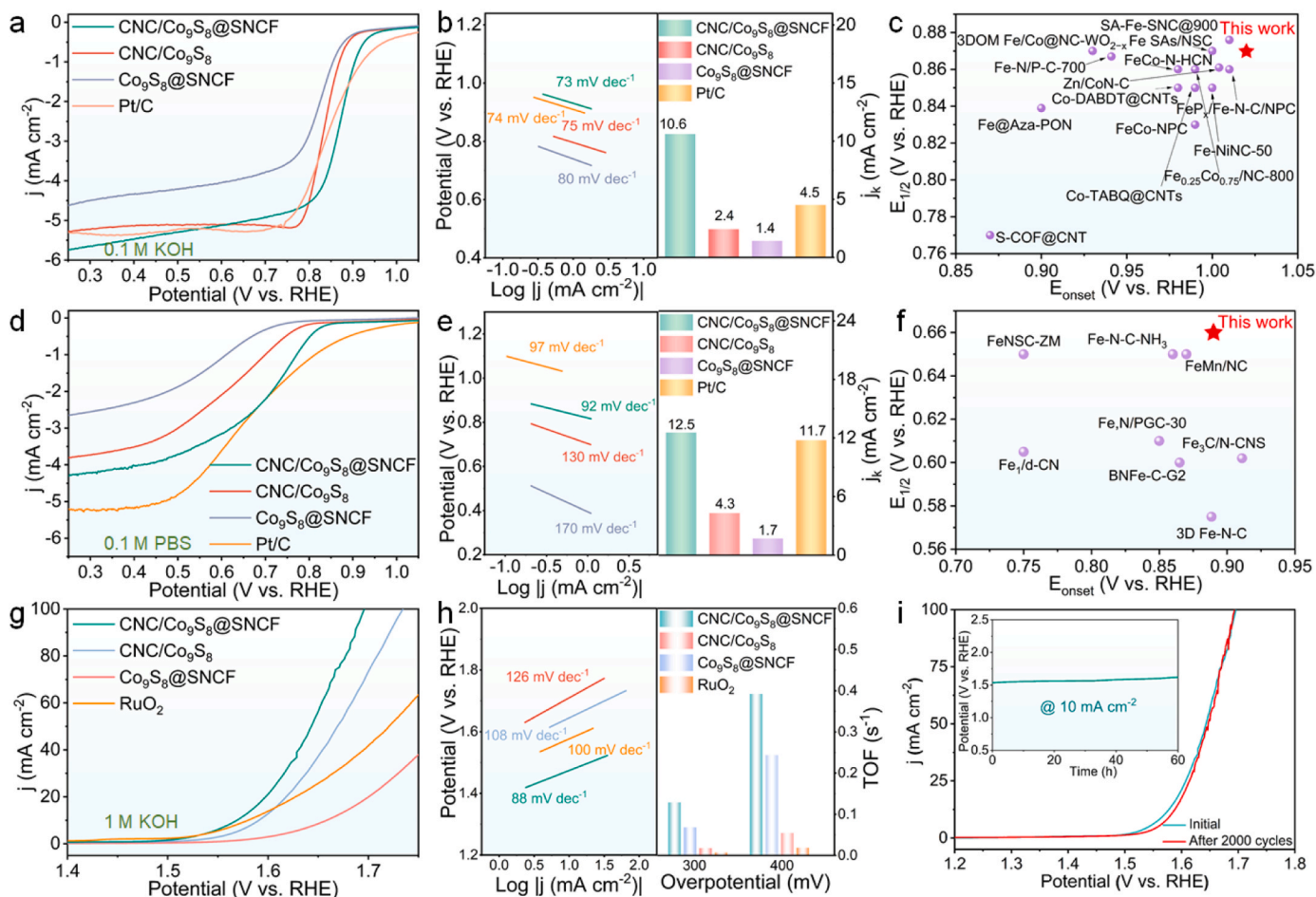

Fig. 2. (a) ORR LSV curves, (b) Tafel plots and J$_k$ for the CNC/Co$_9$S$_8$@SNCF, Co$_9$S$_8$@SNCF, CNC/Co$_9$S$_8$ and Pt/C catalysts in O$_2$-saturated 0.1 M KOH media. (c) Comparison of the performance of CNC/Co$_9$S$_8$@SNCF and other reported catalysts in alkaline solution. (d-f) ORR LSV curves, Tafel plots and J$_k$ and comparison of the performance in 0.1 M PBS solution. (g) OER LSV curves, (h) Tafel plots and TOFs for the CNC/Co$_9$S$_8$@SNCF, Co$_9$S$_8$@SNCF, CNC/Co$_9$S$_8$ and RuO$_2$ catalysts in 1 M KOH solution. (i) OER durability test at 10 mA cm^{-2} and polarization curves before and after 2000 cycles in 1 M KOH solution.

universal media.

The electrocatalytic performance and stability of OER were systematically investigated. The commercial RuO_2 was chosen as the benchmark for OER analysis. Figs. 2g and S18 depict the LSV curves of OER, indicating a notably low overpotential of 340 mV for CNC/Co_9S_8@SNCF at 10 mA cm^{-2}. This OER performance surpasses that of Co_9S_8@SNCF (359 mV), CNC/Co_9S_8 (429 mV) and commercial RuO_2 catalysts (350 mV). Additionally, the corresponding Tafel slope of CNC/Co_9S_8@SNCF is estimated at 88 mV dec^{-1}, lower than that of Co_9S_8@SNCF (108 mV dec^{-1}), CNC/Co_9S_8 (126 mV dec^{-1}) and RuO_2 (100 mV dec^{-1}) (Fig. 2h). Electrochemical impedance spectroscopy (EIS) results and associated parameters are presented in Fig. S19. The CNC/Co_9S_8@SNCF electrode exhibits significantly lower charge transfer resistance value (R_{ct}, 3.71 Ω) compared to the Co_9S_8@SNCF (6.73 Ω) and CNC/Co_9S_8 (6.53 Ω) [45,46]. The observed minimum Tafel slope and R_{ct} for CNC/Co_9S_8@SNCF demonstrate favorable kinetics. The turnover frequencies (TOFs) of catalysts are calculated (Fig. 2h) and reveal that CNC/Co_9S_8@SNCF possesses much higher TOF values at different overpotentials than other control electrocatalysts. Furthermore, the diffusion of the hydroxyl ions during the OER process can be assessed by examining the linear trend in the low-frequency region of the Z' versus $\omega^{-1/2}$ plot. A significantly smaller slope for CNC/Co_9S_8@SNCF compared to Co_9S_8@SNCF and CNC/Co_9S_8 indicates the enhanced transfer of hydroxyl ions (Fig. S20) [47]. This manifestation indicates that multilayer macroporous fibers can provide abundant sites with high intrinsic activity and promote ion diffusion of reactants during the OER process. Furthermore, the CNC/Co_9S_8@SNCF catalyst displays excellent stability under KOH solution, evident in nearly unaltered LSV curves after 2000 CV cycles and a consistent OER current sustained over 60 h at 10 mA cm^{-2} for continuous testing (Fig. 2i). Further assessment of the OER performance for CNC/Co_9S_8@SNCF was conducted under acidic (0.5 M H_2SO_4) and neutral (0.1 M PBS) conditions (Fig. S21), and the overpotentials of 960 mV and 720 mV have been achieved at the current density of 10 mA cm^{-2}, respectively. Additionally, the CNC/Co_9S_8@SNCF catalyst exhibits stability for approximately 15 h in acidic electrolytes and about 60 h in neutral electrolytes.

The pure Co_9S_8 and CNC@SNCF samples were further prepared (Figs. S22 and S23), and their corresponding catalytic performance was measured as shown in Fig. S24. Both Co_9S_8 and CNC@SNCF exhibit relatively poor OER and ORR activities, emphasizing the importance of advantageous structural carriers and efficient active sites. In Fig. S25, the calculated electrochemical double-layer capacitance (C_{dl}) of CNC/Co_9S_8@SNCF is 21.6 mF cm^{-2}, larger than those of Co_9S_8@SNCF (17.5 mF cm^{-2}), CNC/Co_9S_8 (9.5 mF cm^{-2}) and pure Co_9S_8 (2.4 mF cm^{-2}). To reflect the intrinsic electrocatalytic activities, the LSV curves were normalized by electrochemical active surface area (ECSA). The CNC/Co_9S_8@SNCF catalyst shows much better OER activity (Fig. S26) than those of CNC/Co_9S_8, Co_9S_8@SNCF and RuO_2 samples, indicating multilayer macroporous fiber architecture significant for exposing larger active area and enhancing the intrinsic activity of each site [48]. Additionally, based on the Raman analysis from Fig. S27, the I_D/I_G for CNC/Co_9S_8@SNCF exhibits a slightly smaller value among the control samples, suggesting it possesses a higher conductivity and the fewer defect sites over the carbon matrix [49,50]. The potential gap between OER and ORR ($\Delta E = E_{j10} - E_{1/2}$) was studied to understand the bifunctional electrochemical properties. As detailed in Table S6, CNC/Co_9S_8@SNCF exhibits a ΔE of 0.7 V, which is below that of Pt/C-RuO_2 (0.73 V) and most of bifunctional materials reported in the literature. These results demonstrate its advantageous application in RZABs as an advanced oxygen electrocatalyst.

3.3. Performance of liquid RZABs

The considerable ORR and OER activities exhibited by the designed CNC/Co_9S_8@SNCF inspire further exploration of its practical behavior in RZABs. The schematic representation of the liquid RZAB configuration is presented in Fig. 3a, where a Zn plate, 6 M KOH combined with 0.2 M zinc acetate, and CNC/Co_9S_8@SNCF catalyst served as the Zn anode, electrolyte and air cathode, respectively. For comparison, the air electrodes were prepared using Co_9S_8@SNCF, CNC/Co_9S_8 and benchmark Pt/C + RuO_2, respectively. The liquid RZAB based on CNC/Co_9S_8@SNCF achieves an open circuit voltage (OCV) of 1.48 V (Fig. S28), higher than that of Pt/C + RuO_2 (1.44 V). Galvanostatic discharge measurements on the CNC/Co_9S_8@SNCF-based RZAB (Fig. 3b) display a smaller voltage drop at current densities ranging from 10 to 60 mA cm^{-2} compared to Pt/C-based battery (Fig. S29). Meanwhile, the battery based on CNC/Co_9S_8@SNCF demonstrates reversible discharge resumption upon reducing the current density to 10 mA cm^{-2}, indicating excellent rechargeability and discharge rate performance. Furthermore, the CNC/Co_9S_8@SNCF-based battery displays a high specific discharge capacity of 758 mAh g^{-1} based on the consumed mass of Zn anode at 20 mA cm^{-2}, which is comparable to that of Pt/C catalyst (Figs. 3c and S30). Notably, the liquid RZAB based on CNC/Co_9S_8@SNCF achieves a maximum power density of 280 mW cm^{-2}, while Co_9S_8@SNCF, CNC/Co_9S_8 and Pt/C + RuO_2 exhibit lower values of 122, 94 and 127 mW cm^{-2}, respectively (Figs. 3d and S31). The galvanostatic discharge-charge measurements at 10 mA cm^{-2} (Fig. 3e) showed that the voltage gap has no noticeable change after 1200 h (corresponding to 3600 cycles), maintaining a high round-trip efficiency of 59%. However, the Co_9S_8@SNCF and CNC/Co_9S_8-based batteries exhibit poor cycling stability and large voltage gaps under the same operating conditions. To investigate the cause for the differences in cycling stability, the EIS was employed to analyze changes in impedance before and after cycling, as shown in Fig. 3f and Table S7. The ohmic resistance of the Co_9S_8@SNCF and CNC/Co_9S_8-based electrodes increased significantly after the 1000th cycle to 3.90 and 4.45 Ω, respectively. In contrast, the CNC/Co_9S_8@SNCF-based electrode exhibits a comparatively lower resistance of 3.23 Ω after cycling, which suggests that CNC/Co_9S_8@SNCF possesses superior charge and mass transport even after cycling. Furthermore, the morphology and composition of CNC/Co_9S_8@SNCF was maintained during the test (Figs. S32 and S33), providing additional evidence of the outstanding stability of CNC/Co_9S_8@SNCF. The key data parameters of recently reported RZABs are presented in Fig. 3g and Table S8, and the distinct advantages of CNC/Co_9S_8@SNCF-based RZABs, particularly regarding power density and cycle stability, are evident from the comprehensive analysis.

Given the heightened safety profile of neutral electrolytes, we proceeded to construct a liquid RZAB in a neutral solution (4 M NH_4Cl + 2 M KCl). The neutral RZAB based on CNC/Co_9S_8@SNCF displays impressive performance, featuring a high OCV of 1.42 V and good rate performance (Fig. 3h and i). Analysis of the charge-discharge curves reveals the voltage gap of the CNC/Co_9S_8@SNCF-based battery is lower than that of Pt/C + RuO_2 at the same current density (Fig. 3j). Meanwhile, the corresponding peak power density reaches 46 mW cm^{-2}, surpassing that of Pt/C + RuO_2 (33 mW cm^{-2}) and most reported neutral ZABs (Table S9). Additionally, the discharging-charging curve of the neutral RZAB exhibits sustained performance for over 3000 min at 10 mA cm^{-2} (Fig. S34).

3.4. The impact of structure on interface microenvironment

The charging and discharging processes of RZAB involve complex three-phase interfaces, where mass transport between the reactant and active sites becomes a crucial factor governing the reaction rate. Consequently, a comprehensive exploration of the interfacial microenvironment for the CNC/Co_9S_8@SNCF catalyst can provide deeper insights for battery performance enhancement. Nitrogen adsorption/desorption isotherms were measured to evaluate the porous properties and pore size distribution of the prepared samples. As shown in Fig. 4a, CNC/Co_9S_8@SNCF exhibits the Brunaner-Emmett-Teller (BET) specific
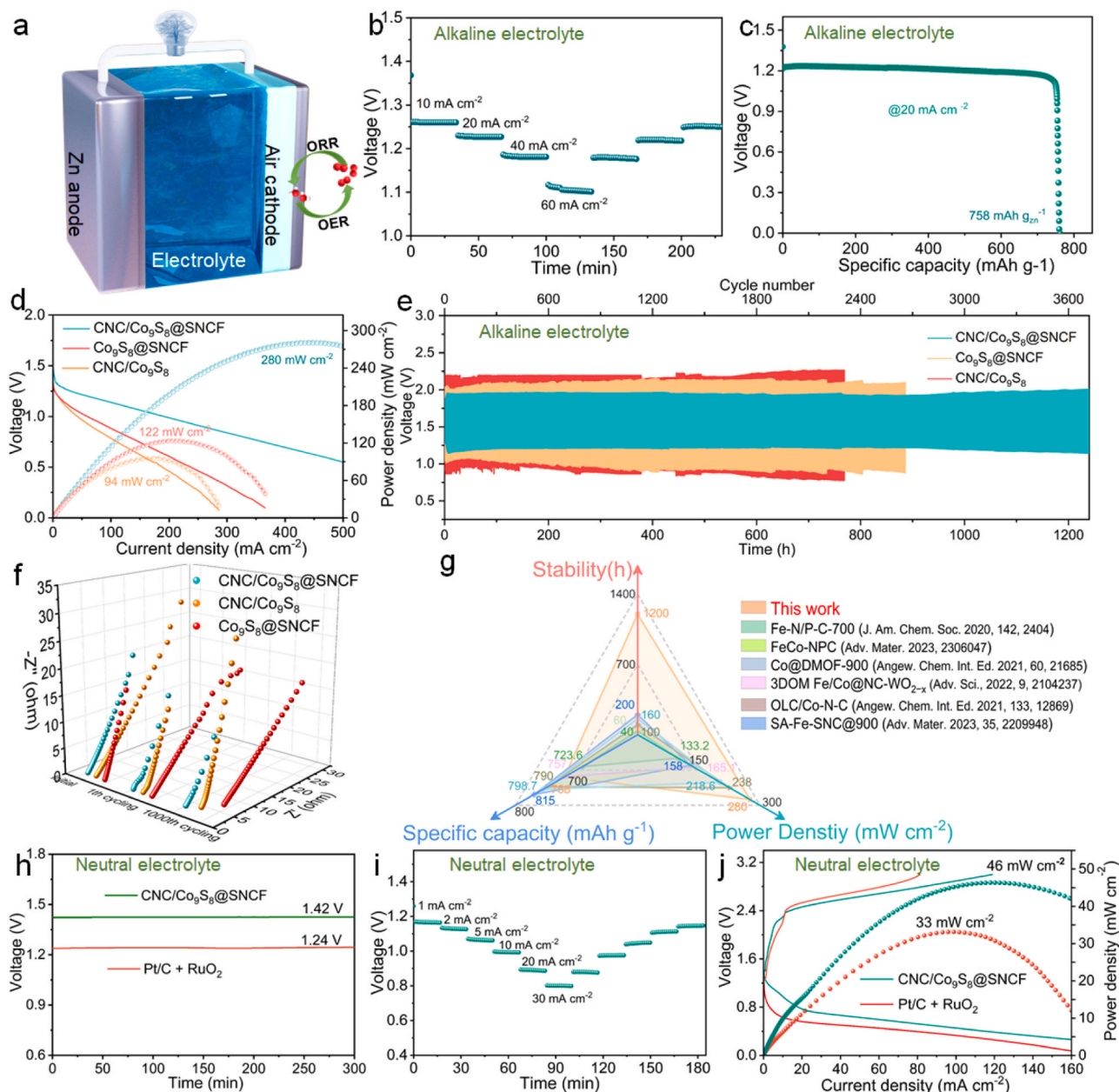
Fig. 3. (a) Schematic illustration of liquid RZAB configuration. (b) Discharge curves at different current densities and (c) discharge specific capacity curve at 20 mA cm^{-2} of the CNC/Co$_9$S$_8$@SNCF-based RZABs. (d) Discharge polarization and power density curves, (e) galvanostatic discharge-charge cycling curves and (f) EIS curves tested at the 0th, 1th and 1000th cycles of the CNC/Co$_9$S$_8$@SNCF, Co$_9$S$_8$@SNCF and CNC/Co$_9$S$_8$-based RZABs under alkaline electrolytes. (g) Performance comparison of CNC/Co$_9$S$_8$@SNCF and other air electrodes reported recently. (h) OCV curves, (i) discharge curves at different current densities, (j) charge-discharge and power density curves of the Co$_9$S$_8$/Co@HSNCF and Pt/C + RuO$_2$-based RZABs under neutral electrolytes.

surface area of 122.8 m^3 g^{-1}, which is greater than that of Co$_9$S$_8$@SNCF (35.6 m^3 g^{-1}). Moreover, CNC/Co$_9$S$_8$@SNCF demonstrates a significantly larger pore volume of 0.33 cm^3 g^{-1}, in contrast to Co$_9$S$_8$@SNCF (0.11 cm^3 g^{-1}). This increased BET surface area and pore volume facilitate ion diffusion and gas adsorption within the bulk phase, providing numerous active sites for electrochemical reactions.

During the ORR electrocatalysis process, the diffusion of the resulting OH$^-$ near the catalyst is directly correlated with the local pH value, and alterations in pH exert significant influence on catalytic kinetics. To quantitatively estimate the local pH near the CNC/Co$_9$S$_8$@SNCF and Co$_9$S$_8$@SNCF catalysts at different applied potentials, we employ a RuO$_x$-modified RRDE technique [51]. The OCP vs. pH plot was generated for different electrolytic pH values, and their corresponding OCP is shown in Fig. S35. Fig. 4b depicts the local pH changes induced by

different catalysts with applied potential in 0.1 M KOH electrolytes. Notably, CNC/Co$_9$S$_8$@SNCF exhibits a slower rate of increase in local pH at the ORR test potential, indicating faster diffusion of OH$^-$ ions. This behavior may be attributed to the increased specific surface area, which facilitates an expanded interface between the liquid and catalyst surface, and slows down the accumulation of OH$^-$ at the local catalyst sites [52, 53]. The dynamic excessive increase in local pH during ORR can cause an enhanced the selectivity of 2e-ORR pathway and a Nernstian concentration loss, ultimately reducing the cell output voltage [54].

Furthermore, O$_2$ temperature-programmed desorption (O$_2$-TPD) spectra were carried out to investigate the adsorption of oxygen molecules on the catalyst surface. As revealed in Fig. 4c, CNC/Co$_9$S$_8$@SNCF shows more pronounced peaks related to O$_2$ physisorption than Co$_9$S$_8$@SNCF in the range of 100–200 °C. This enhanced O$_2$ desorption

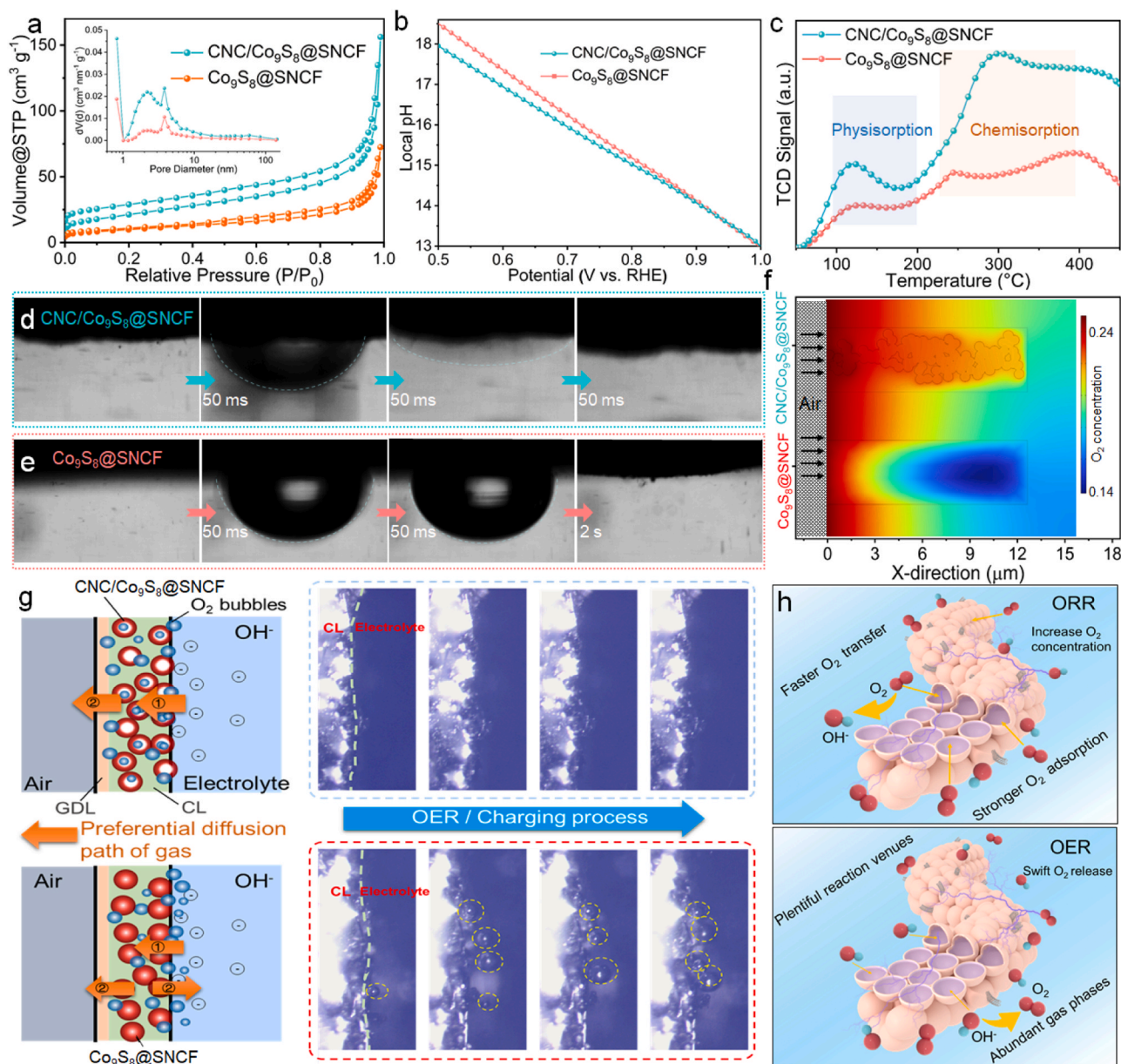**Fig. 4.** (a) N_2 sorption isotherm and pore size distribution of the CNC/Co_9S_8@SNCF and Co_9S_8@SNCF. (b) The variation of local pH value with applied potential. (c) O_2-TPD curves. O_2 bubbles adhesion behavior evolution on the surfaces of (d) CNC/Co_9S_8@SNCF and (e) Co_9S_8@SNCF electrodes in O_2-saturated KOH solution. (f) COMSOL Multiphysics Modeling of O_2 diffusion into the air electrode. (g) In-situ electrode surface of CNC/Co_9S_8@SNCF and Co_9S_8@SNCF-based RZABs at a current density of 10 mA cm^{-2} over 20 min. (h) Illustration of the catalytic process and mechanism for ORR and OER in CNC/Co_9S_8@SNCF.

signal results from the favorable macroporous architecture, promoting O_2 trapping and physisorption. In the temperature range from 230 to 400 °C, CNC/Co_9S_8@SNCF delivers the reinforced signal compared to Co_9S_8@SNCF, confirming the increase in O_2 chemisorption. The previous study suggests that electron transfer from the surface to the oxygen molecule is essential for oxygen chemisorption, with the metal-support interface contributing to the activation of O_2 [55]. The large specific surface area of the CNC/Co_9S_8@SNCF promotes the exposure of Co_9S_8 active sites within curved carbon, with each exhibiting stronger adsorption capacity, thereby enhancing the capacity of chemisorbed O_2 [56]. Contact angle measurements reveal high contact angle values of 125° and 123° on CNC/Co_9S_8@SNCF and Co_9S_8@SNCF, respectively (Fig. S36), demonstrating the hydrophobic nature of both electrodes. Additionally, O_2 adhesion experiments confirm the aerophilic character of electrodes, as O_2 bubbles liberated from the electrolyte immediately diffuse over the CNC/Co_9S_8@SNCF electrode in mere 50 ms (Fig. 4d).

Conversely, O_2 bubbles released from the solution remain attached to the surface of Co_9S_8@SNCF for up to 2 s (Fig. 4e), indicating hindered O_2 diffusion across the interface. Consequently, while both CNC/Co_9S_8@SNCF and Co_9S_8@SNCF exhibit hydrophobic properties, the multilayer macroporous nanostructure of carbon fibers facilitates enhanced O_2 adsorption and faster O_2 transfer. To further elucidate the distribution of O_2 within the air electrode, a reaction diffusion model was constructed employing the COMSOL multiphysics FEM solver [57]. The diffusion of air (oxygen) in CNC/Co_9S_8@SNCF and Co_9S_8@SNCF was simulated, and the resulting gaseous oxygen concentration contour plot is depicted in Fig. 4f. Evidently, electrode geometries resembling CNC/Co_9S_8@SNCF in morphology exhibit reduced gaseous oxygen transfer resistance, leading to higher O_2 concentration within the internal carbon nanocapsules. Conversely, Co_9S_8@SNCF tends to obstruct the O_2 diffusion pathway into the interior of the catalyst, resulting in relatively low oxygen concentration. Therefore, we can infer that

continuous carbon nanocapsule frame electrodes can improve the utilization of gas-phase O_2, thus improving the performance of RZAB.

In a liquid environment, excess energy is required to drive the generated O_2 bubbles with ultra-small radius according to Kelvin's equation, thereby increasing overpotential for the OER. Consequently, in situ optical microscopy was employed to investigate the cross section of the electrodes during the gas generation process associated with battery charging. As illustrated in Fig. 4g, almost no obvious bubbles are observed at the CNC/Co$_9$S$_8$@SNCF electrode, whereas bubble generation is evident at the Co$_9$S$_8$@SNCF electrode. This observation aligns with the literature [58], which suggests that the O_2 molecules preferentially transfer to the available gas phase rather than accumulate to yield bubbles. The CNC/Co$_9$S$_8$@SNCF with macroporous structure provides plentiful gas seeds, causing O_2 generated during the OER process to preferentially diffuse towards the pores and be stored within the material. In the air cathode, O_2 passes in and out of the cell through the gas diffusion layer (GDL) and the catalyst layer (CL). According to reports, the transport mechanism of O_2 through CL is dominated by Knudsen diffusion and molecular diffusion, while GDL is characterized by molecular diffusion [59]. Meanwhile, the effective diffusion coefficient of O_2 in CL composed of CNC/Co$_9$S$_8$@SNCF is calculated as 5.12×10^{-7} cm^{-2} s^{-1} (Fig. S37), which far exceeds that in KOH solution. Therefore, the stored oxygen from the macroporous carbon nanocapsules of catalyst is easily released into the air through the GDL, reducing the overpotential during the OER process. In contrast, the Co$_9$S$_8$@SNCF electrode shows more obvious bubble evolution, which may be due to insufficient oxygen adsorption and storage performance, causing part of the O_2 bubbles to be generated at electrolyte interface.

Based on the experimental analysis, the noticeable bifunctional activities of CNC/Co$_9$S$_8$@SNCF can be depicted in Fig. 4h. The extensive specific surface area and continuous carbon nanocapsule structure of carbon fibers optimize the local interfacial environment of the catalyst, making it more suitable for ORR and OER. Specifically, CNC/Co$_9$S$_8$@SNCF offers numerous channels for O_2 transfer, facilitating O_2 storage and enhancing O_2 concentration at three-phase reaction interface, thereby improving ORR kinetics. Simultaneously, the accumulation of OH$^-$ at the catalyst site is reduced and increase in local pH is slowed down, which promotes the selectivity of 4e-ORR. In the OER process, the macroporous carbon fibers create abundant places for active sites to contact the electrolyte/electrons, allowing for rapid transport of OH$^-$. The presence of numerous gas phases in CNC/Co$_9$S$_8$@SNCF accelerates the swift release of produced O_2 species and circumvents the energy consuming bubble formation process, ultimately reducing the OER overpotential.

3.5. Catalytic mechanism study and DFT calculation

To achieve understanding of the catalytic sites for ORR and OER within CNC/Co$_9$S$_8$@SNCF, potassium thiocyanate (KSCN) poisoning and in situ characterization techniques were carried out. Introducing
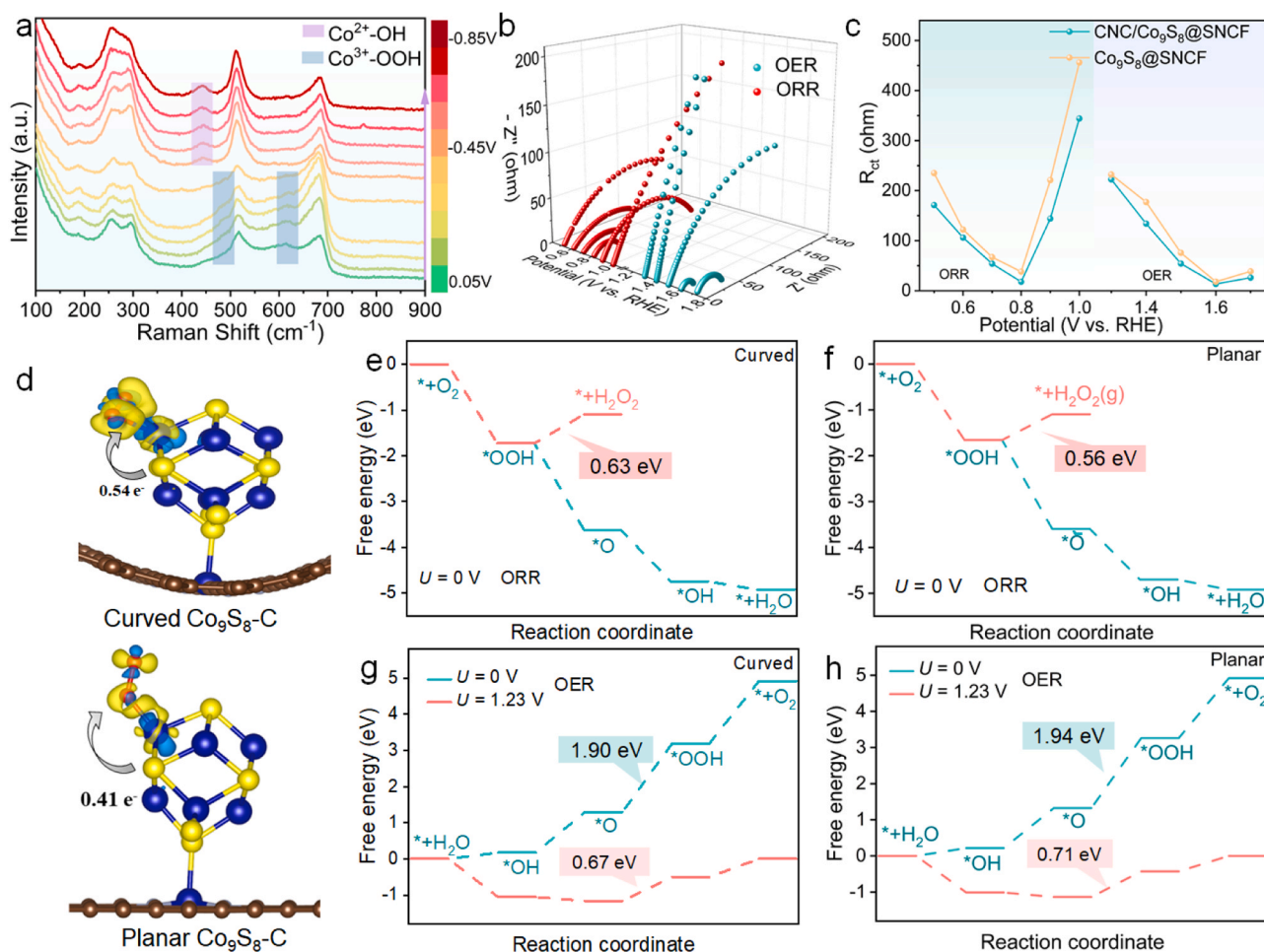

Fig. 5. (a) In situ Raman spectra of the CNC/Co$_9$S$_8$@SNCF recorded in O_2-saturated 0.1 M KOH at room temperature. (b) Nyquist plots of the CNC/Co$_9$S$_8$@SNCF at different applied potentials in KOH solution. (c) Response of the R$_{ct}$ at different potentials for CNC/Co$_9$S$_8$@SNCF and Co$_9$S$_8$@SNCF. (d) Charge density difference and Bader charge analysis of O_2 adsorbed on curved Co$_9$S$_8$-C and planar Co$_9$S$_8$-C. ORR free energy diagrams of (e) curved Co$_9$S$_8$-C and (f) planar Co$_9$S$_8$-C at $U = 0$ V. OER free energy diagrams of (g) curved Co$_9$S$_8$-C and (h) planar Co$_9$S$_8$-C at $U = 0$ V and $U = 1.23$ V.

10 mM KSCN into the electrolyte disrupts and potentially inhibits reactions accelerated by Co-involved species due to the strong coordination between metal ions and SCN⁻ ions [60]. As shown in Fig. S38, CNC/Co$_9$S$_8$@SNCF displays significant drop in ORR performance, while OER activity almost disappeared following the addition of KSCN [61]. This result suggests that the ORR activity of CNC/Co$_9$S$_8$@SNCF is mainly influenced by Co$_9$S$_8$ and the S, N codoped carbon matrix, whereas the OER performance is controlled by the Co$_9$S$_8$ sites [62]. Moreover, the in situ Raman spectroscopy is performed to monitor the intermediate adsorption/desorption on active sites and unravel the actual active sites for ORR process. Fig. 5a shows the in situ Raman spectra with an applied potential range from −0.05 V to −0.85 V on CNC/Co$_9$S$_8$@SNCF. At the beginning of ORR process, two peaks are observed at 475 cm⁻¹ and 613 cm⁻¹ corresponding to Co^{III}-OOH, and 475 cm⁻¹ refers to the E$_g$ (Co-O stretching mode) of Co-OOH, indicating the transformation from the absorbed oxygen to *OOH intermediate on Co^{III} sites [63,64]. As the potential decreases, the two peaks corresponding to Co-OOH gradually disappear and a new peak referring to Co^{II}-OH appears instead at 446 cm⁻¹, which is due to the conversion of Co^{III}-OOH to Co^{II}-OH species during ORR [65]. Therefore, the ORR mechanism is proposed that the O$_2$ is first adsorbed on the main catalytic sites (Co^{3+}) to form Co^{III}-OOH and then Co^{III}-OOH species interact with OH⁻ to generate Co^{II}-OH, and finally the OH intermediate desorption occurs.

To clarify the charge transfer kinetics during the potential-dependent evolution, we investigated the EIS spectra of CNC/Co$_9$S$_8$@SNCF and Co$_9$S$_8$@SNCF, varying applied potential in accordance with OER and ORR performance (Figs. 5b and S39). The changing trend and diameter of the semicircle in the Nyquist plots reveal faster kinetics and adsorption of reactants with increasing potentials. In Fig. 5c, the R$_{ct}$ of CNC/Co$_9$S$_8$@SNCF is smaller than that of Co$_9$S$_8$@SNCF during both OER and ORR processes, implying faster adsorption kinetics of key intermediates, specifically oxygen-containing species. Previous investigations have confirmed that with respect to the hollow carbon nanostructures, the stress variation of curvature structure can distort the planar structure of the sp^2-hybridized carbon, causing a shift of the π-electron density from the concave to convex surface [66]. This π-electron density shift directly influences the electronic behavior of the metal species loaded on the concave carbon surface by the modulated charge transfer mechanism [67], a phenomenon consistent with the obvious shift in Co 2p binding energy observed between CNC/Co$_9$S$_8$@SNCF and Co$_9$S$_8$@SNCF. Correspondingly, the regulated electronic metal-support interaction optimizes the adsorption energy of reaction intermediates, thus affecting the catalytic performance.

To gain deeper insights into catalytic mechanism, we constructed a simplified theoretical model to explore the impact of the electronic interaction on reaction intermediates through DFT calculations. The carbon nanocapsule-loaded active sites was simulated by embedding Co$_9$S$_8$ sites within curved carbon, and the verified structure of curved Co$_9$S$_8$-C and planar Co$_9$S$_8$-C is presented in Fig. S40. Charge density difference and Bader charge analysis reveal a greater extent of charge transfer from Co$_9$S$_8$ NPs to curved carbon compared to planar carbon (Fig. S41), consistent with XPS results. This observation validates the viability of the simplified model. Furthermore, as depicted in Fig. 5d, the adsorbed O$_2$ species obtained a higher amount of charge (0.54 e⁻) from the Co site in curved Co$_9$S$_8$-C than planar Co$_9$S$_8$-C (0.4 e⁻). This finding was further confirmed by the adsorption energy results (Fig. S42). The adsorption energies of O$_2$ in curved Co$_9$S$_8$-C and planar Co$_9$S$_8$-C are calculated to be −1.39 and −1.25 eV, respectively, indicating that O$_2$ adsorption and activation preferentially occur on the curved Co$_9$S$_8$-C. The calculated free energy diagrams of the ORR and OER on curved Co$_9$S$_8$-C and planar Co$_9$S$_8$-C are displayed in Fig. 5e-h. The optimized geometries of curved Co$_9$S$_8$-C and planar Co$_9$S$_8$-C with adsorbed oxygen intermediates are presented in Figs. S43 and S44. The ORR free energies of the two models at zero electrode potential ($U = 0$ V versus RHE) revealed a thermodynamically spontaneous process (Fig. 5e and f). The theoretical limiting potentials of curved Co$_9$S$_8$-C and planar Co$_9$S$_8$-C are

close, however, the reduction of OOH* to H$_2$O$_2$ is endothermic by 0.63 eV on the curved Co$_9$S$_8$-C structure, higher than that of planar Co$_9$S$_8$-C (0.56 eV), indicating that the 2e- reduction pathway is greatly suppressed and curved Co$_9$S$_8$-C would have high selectivity for the 4e- reduction process. The DFT calculations were further conducted to deepen insight into the OER behavior of Co$_9$S$_8$-C and planar Co$_9$S$_8$-C (Fig. 5g and h). At $U = 0$ V, the limiting step of the two models is the transformation from *O to *OOH, curved Co$_9$S$_8$-C shows the free energy difference of 1.90 eV, which is less than that of 1.94 eV for planar Co$_9$S$_8$-C. At $U = 1.23$ V, the potential-limiting step is also the transformation from *O to *OOH and the corresponding values are 0.67 and 0.71 eV for curved Co$_9$S$_8$-C and planar Co$_9$S$_8$-C, respectively. From these results, it can be concluded that the loading of Co$_9$S$_8$ sites in the curved carbon can significantly lower the energy barrier to promote intrinsic OER performance. According to DFT calculations, the electronic effect between Co$_9$S$_8$ sites and carbon nanocapsule can facilitate the selectivity to generate H$_2$O for the 4e-ORR and accelerate the transformation from *O to *OOH for OER. Taken together, these results validate that CNC/Co$_9$S$_8$@SNCF possesses excellent oxygen electrocatalytic activities for ORR and OER.

3.6. Performance of flexible RZABs

Flexible wearable electronics are becoming increasingly prevalent in daily life [68,69], and inspired by this trend, we constructed both sandwich-shaped and fiber-shaped flexible RZABs to explore the potential of wearable technology. The sandwich-shaped quasi-solid state alkaline flexible RZAB, depicted in Fig. 6a, incorporated CNC/Co$_9$S$_8$@SNCF as the air cathode, Zn foil as the anode, and polyvinyl alcohol (PVA)-KOH electrolyte. The flexible battery exhibits a high OCV of 1.42 V and has the capacity to power small electric motors, as shown in Fig. 6b. Furthermore, Fig. 6c illustrates that the flexible battery shows a charge-discharge voltage gap at 50 mA cm⁻² of 0.89 V and achieves a peak power density as high as 159 mW cm⁻², which is superior to that of the reported quasi-solid state alkaline RZABs (Table S10). In Fig. 6d, the round-trip voltage gap of the flexible battery slightly increases from 0.73 V (round-trip efficiency of 62%) to 0.76 V (round-trip efficiency of 60%) during continuous cycling for 26 h, indicating its long-term cycling stability and good rechargeability. In addition, the sandwich-shaped flexible battery possesses high mechanical flexibility, and operates steadily at different bending angles from 0° to 120° (Fig. 6e). A fiber-type flexible battery with polyacrylic acid (PAA)-KOH gel was further assembled (Fig. 6f), demonstrating excellent resistance to deformation and the ability to flex into various states without any structural damage (Fig. 6g). A single CNC/Co$_9$S$_8$@SNCF-- driven flexible fiber-type battery exhibits an OCV of 1.39 V and a peak power density of 40 mW cm⁻² (Figs. 6h and S45) and the assembled fibrous batteries can effectively power a watch (Fig. 6i), highlighting its potential applications in flexible wearable devices.

4. Conclusion

In summary, we have prepared a multilayer macroporous carbon fibers electrocatalyst through a structural engineering strategy, which is an advanced bifunctional oxygen electrocatalyst, exhibiting high ORR and OER performance, superior to most reported noble-metal-based materials. Experimental and characterization results reveal that the internal carbon nanocapsule layer functions as a "gas buffer", while the outer fiber support establishes a 3D framework that enhances electron mass transfer. The interfacial microenvironment of the active sites is effectively regulated and the gas diffusion and ion mass transfer during the ORR and OER processes are promoted. Calculation results further reveal that the curved structure of carbon nanocapsules loaded with Co$_9$S$_8$ NPs promotes the four-electron selectivity of ORR, and reduces the energy barrier for OER reaction. Notably, the assembled liquid RZABs exhibit a high power density (280 mW cm⁻²), specific capacity
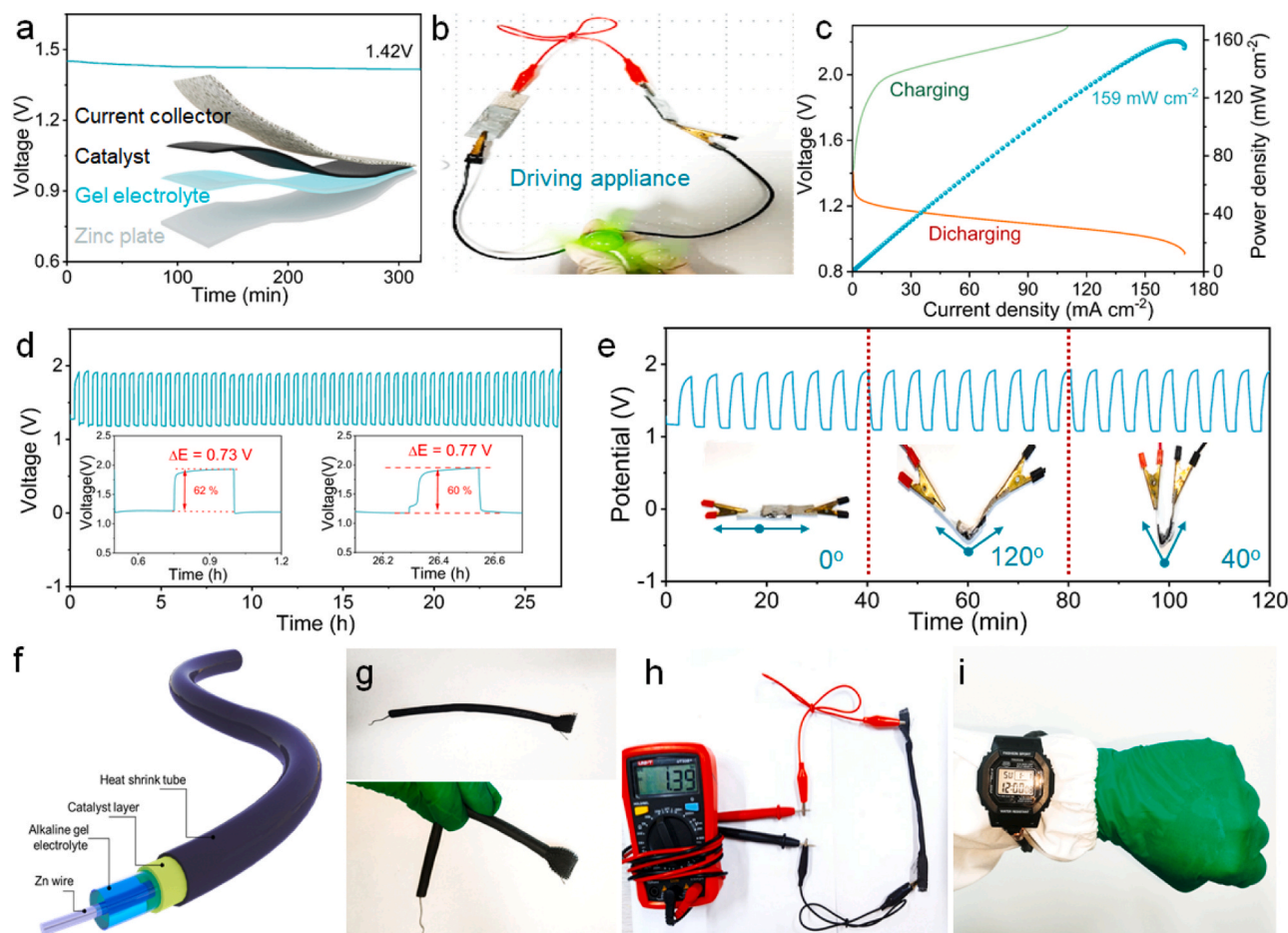
Fig. 6. (a) Scheme and OCV curve of a sandwich-shaped quasi-solid state alkaline flexible RZAB. (b) Digital photos show the application of flexible RZABs. (c) Polarization curves and corresponding power density curve of CNC/Co$_9$S$_8$@SNCF -based flexible RZAB. (d) charge-discharge cycling curve. (e) Charge and discharge curve under different bending angles of sandwich-shaped flexible RZAB. (f) Schematic diagram of the assembly of a flexible fiber-type RZAB. (g) Demonstration of the fibrous battery under straight and knotted form. (h) OCV of fibrous battery. (i) The photographs of an electronic clock powered by fibrous battery.

(758 mAh g^{-1}) and cycle stability (1200 h), and the flexible quasi-solid state RZABs also exhibit high power density, good rechargeability and broad applicability. These findings provide new insights into the design of electrocatalysts for metal-air battery systems by optimizing the interfacial microenvironment.

CRediT authorship contribution statement

Jiqiang Ning: Writing – review & editing, Formal analysis. **Yijing Gao:** Visualization, Software, Validation. **Yong Hu:** Writing – review & editing, Supervision, Project administration, Funding acquisition, Conceptualization. **Chen Yang:** Writing – original draft, Data curation, Conceptualization. **Lei Yan:** Methodology, Formal analysis, Data curation, Writing – original draft. **Jie Chen:** Methodology, Investigation, Formal analysis.

Declaration of Competing Interest

The authors declared that there is no conflict of interest.

Data availability

The authors do not have permission to share data.

Appendix A. Supporting information

Supplementary data associated with this article can be found in the online version at doi:10.1016/j.apcatb.2024.124060.

References

[1] W. Sun, F. Wang, B. Zhang, M. Zhang, V. Kupers, X. Ji, C. Theile, P. Bieker, K. Xu, C. Wang, M. Winter, A rechargeable zinc-air battery based on zinc peroxide chemistry, Science 371 (2021) 46–51.
[2] H. Sun, X. Xu, H. Kim, Z. Shao, W. Jung, Advanced electrocatalysts with unusual active sites for electrochemical water splitting, InfoMat 6 (2023) 12494.
[3] M. Haq, D. Wu, Z. Ajmal, Q. Ruan, S. Khan, L. Zhang, A. Wang, J. Feng, Derived-2D Nb$_4$C$_3$T$_x$ sheets with interfacial self-assembled Fe-N-C single-atom catalyst for electrocatalysis in water splitting and durable zinc-air battery, Appl. Catal. B: Environ. 344 (2024) 123632.
[4] X. Xiao, L. Zou, H. Pang, Q. Xu, Synthesis of micro/nanoscaled metal-organic frameworks and their direct electrochemical applications, Chem. Soc. Rev. 49 (2020) 301–331.

[5] J. Song, C. Wei, Z. Huang, C. Liu, L. Zeng, X. Wang, Z.J. Xu, A review on fundamentals for designing oxygen evolution electrocatalysts, Chem. Soc. Rev. 49 (2020) 2196–2214.

[6] L. Yan, Z. Xu, X. Liu, S. Mahmood, J. Shen, J. Ning, S. Li, Y. Zhong, Y. Hu, Integrating trifunctional Co@NC-CNTs@NiFe-LDH electrocatalysts with arrays of porous triangle carbon plates for high-power-density rechargeable Zn-air batteries and self-powered water splitting, Chem. Eng. J. 446 (2022) 137049.

[7] Q. Wang, S. Kaushik, X. Xiao, Q. Xu, Sustainable zinc-air battery chemistry: advances, challenges and prospects, Chem. Soc. Rev. 52 (2023) 6139–6190.

[8] Z. Sun, Y. Ding, C. Wang, P. Mao, B. Wang, R. Ran, W. Zhou, K. Liao, Z. Shao, A magnetic binder-linked air electrode with anti-pulverization behavior for rechargeable and recyclable Zn-air batteries, Adv. Funct. Mater. 33 (2023) 202302234.

[9] Y. Pan, X. Ma, M. Wang, X. Yang, S. Liu, H.C. Chen, Z. Zhuang, Y. Zhang, W. C. Cheong, C. Zhang, X. Cao, R. Shen, Q. Xu, W. Zhu, Y. Liu, X. Wang, X. Zhang, W. Yan, J. Li, H.M. Chen, C. Chen, Y. Li, Construction of N, P co-doped carbon frames anchored with Fe single atoms and Fe₂P nanoparticles as a robust coupling catalyst for electrocatalytic oxygen reduction, Adv. Mater. 34 (2022) 2203621.

[10] X. Zhong, Y. Shao, B. Chen, C. Li, J. Sheng, X. Xiao, B. Xu, J. Li, H. Cheng, G. Zhou, Rechargeable zinc-air batteries with an ultra-large discharge capacity per cycle and an ultra-long cycle life, Adv. Mater. 35 (2023) 2301952.

[11] X. Zhao, X. Yu, S. Xin, S. Chen, C. Bao, W. Xu, J. Xue, B. Hui, J. Zhang, X. She, D. Yang, Enhanced oxygen reduction reaction for Zn-air battery at defective carbon fibers derived from seaweed polysaccharide, Appl. Catal. B: Environ. 301 (2022) 120785.

[12] Q. Lu, H. Wu, X. Zheng, Y. Cao, J. Li, Y. Wang, H. Wang, C. Zhi, Y. Deng, X. Han, W. Hu, Controllable constructing janus homologous heterostructures of transition metal alloys/sulfides for efficient oxygen electrocatalysis, Adv. Energy Mater. 12 (2022) 2202215.

[13] Q. Lu, H. Wu, X. Zheng, Y. Chen, A. Rogach, X. Han, Y. Deng, W. Hu, Encapsulating cobalt nanoparticles in interconnected N-doped hollow carbon nanofibers with enriched Co-N-C moiety for enhanced oxygen electrocatalysis in Zn-air batteries, Adv. Sci. 8 (2021) 2101438.

[14] S. Li, S. Wang, J. He, K. Li, Y. Xu, M. Wang, S. Zhao, Y. Wang, X. Li, X. Zhong, J. Wang, Chromium-doped nickel oxide and nickel nitride mediate selective electrocatalytic oxidation of sterol intermediates coupled with H₂ evolution, Angew. Chem. Int. Ed. 62 (2023) 202306553.

[15] X. Xu, Y. Pan, Y. Zhong, R. Ran, Z. Shao, Ruddlesden-Popper perovskites in electrocatalysis, Mater. Horiz. 7 (2020) 2519–2565.

[16] L. Yan, J. Chen, C. Yang, J. Ning, Y. Hu, Achieving high energy efficiency: Recent advances in Zn-air-based hybrid battery systems, Small Sci. 4 (2023) 2300094.

[17] J. Zhang, X. Dong, G. Wang, J. Chen, R. Wang, Interfacial engineering-induced Janus heterostructures with enhanced electronic regulation for efficient oxygen electrocatalysis in rechargeable Zn-air batteries, Appl. Catal. B: Environ. 342 (2024) 123459.

[18] X. Zhang, X. Xu, S. Yao, C. Hao, C. Pan, X. Xiang, Z. Tian, P. Shen, Z. Shao, S. Jiang, Boosting electrocatalytic activity of single atom catalysts supported on nitrogen-doped carbon through N coordination environment engineering, Small 18 (2022) 2105329.

[19] S. Lee, J. Choi, M. Kim, J. Park, M. Park, J. Cho, Material design and surface chemistry for advanced rechargeable zinc-air batteries, Chem. Sci. 13 (2022) 6159–6180.

[20] J. Liu, C. Zhao, J. Wang, D. Ren, B. Li, Q. Zhang, A brief history of zinc-air batteries: 140 years of epic adventures, Energy Environ. Sci. 15 (2022) 4542–4553.

[21] C. Weng, X. Lv, J. Ren, T. Ma, Z. Yuan, Engineering gas-solid-liquid triple-phase interfaces for electrochemical energy conversion reactions, Electrochem. Energy Rev. 5 (2022) 19.

[22] S. Yu, S. Louisia, P. Yang, The interactive dynamics of nanocatalyst structure and microenvironment during electrochemical CO₂ conversion, JACS Au 2 (2022) 562–572.

[23] M. Xu, D. Li, K. Sun, L. Jiao, C. Xie, C. Ding, H. Jiang, Interfacial microenvironment modulation boosting electron transfer between metal nanoparticles and MOFs for enhanced photocatalysis, Angew. Chem. Int. Ed. 60 (2021) 16372–16376.

[24] W. Tian, J. Ren, X. Lv, Z. Yuan, A "gas-breathing" integrated air diffusion electrode design with improved oxygen utilization efficiency for high-performance Zn-air batteries, Chem. Eng. J. 431 (2022) 133210.

[25] J. Zhong, K. Yan, J. Yang, W. Yang, X. Yang, Microenvironment alters the oxygen reduction activity of Metal/N/C catalysts at the triple-phase boundary, ACS Catal. 12 (2022) 9003–9010.

[26] K. Shi, Z.S. Parsons, X. Feng, Sensitivity of gas-evolving electrocatalysis to the catalyst microenvironment, ACS Energy Lett. 8 (2023) 2919–2926.

[27] Q. Cao, L. Wan, Z. Xu, W. Kuang, H. Liu, X. Zhang, W. Zhang, Y. Lu, Y. Yao, B. Wang, K. Liu, A fluorinated covalent organic framework with accelerated oxygen transfer nanochannels for high-performance zinc-air batteries, Adv. Mater. 35 (2023) 2210550.

[28] T. Zhou, H. Shan, H. Yu, C. Zhong, J. Ge, N. Zhang, W. Chu, W. Yan, Q. Xu, H. Wu, C. Wu, Y. Xie, Nanopore confinement of electrocatalysts optimizing triple transport for an ultrahigh-power-density zinc-air fuel cell with robust stability, Adv. Mater. 32 (2020) 2003251.

[29] L. Wan, Z. Xu, Q. Cao, Y. Liao, B. Wang, K. Liu, Nanoemulsion-coated Ni-Fe hydroxide self-supported electrode as an air-breathing cathode for high-performance zinc-air batteries, Nano Lett. 22 (2022) 4535–4543.

[30] C. Hou, L. Zou, L. Sun, K. Zhang, Z. Liu, Y. Li, C. Li, R. Zou, J. Yu, Q. Xu, Single-atom iron catalysts on overhang-eave carbon cages for high-performance oxygen reduction reaction, Angew. Chem. Int. Ed. 59 (2020) 7384–7389.

[31] L. Yan, B. Xie, C. Yang, Y. Wang, J. Ning, Y. Zhong, Y. Hu, Engineering self-supported hydrophobic-aerophilic air cathode with CoS/Fe₃S₄ nanoparticles embedded in S, N co-doped carbon plate arrays for long-life rechargeable Zn-air batteries, Adv. Energy Mater. 13 (2023) 2204245.

[32] G. Han, X. Zhang, W. Liu, Q. Zhang, Z. Wang, J. Cheng, T. Yao, L. Gu, C. Du, Y. Gao, G. Yin, Substrate strain tunes operando geometric distortion and oxygen reduction activity of CuN₂C₂ single-atom sites, Nat. Commun. 12 (2021) 6335.

[33] Z. Liang, N. Kong, C. Yang, W. Zhang, H. Zheng, H. Lin, R. Cao, Highly curved nanostructure-coated Co, N-doped carbon materials for oxygen electrocatalysis, Angew. Chem. Int. Ed. 60 (2021) 12759–12764.

[34] J. Yang, Z. Wang, C.X. Huang, Y. Zhang, Q. Zhang, C. Chen, J. Du, X. Zhou, Y. Zhang, H. Zhou, L. Wang, X. Zheng, L. Gu, L.M. Yang, Y. Wu, Compressive strain modulation of single iron sites on helical carbon support boosts electrocatalytic oxygen reduction, Angew. Chem. Int. Ed. 60 (2021) 22722–22728.

[35] Q. Lu, J. Yu, X. Zou, K. Liao, P. Tan, W. Zhou, M. Ni, Z. Shao, Self-catalyzed growth of Co, N-codoped CNTs on carbon-encased CoSₓ surface: A noble-metal-free bifunctional oxygen electrocatalyst for flexible solid Zn-air batteries, Adv. Funct. Mater. 29 (2019) 1904481.

[36] M. Guo, Y. Liu, S. Dong, X.L. Jiao, T. Wang, D. Chen, Co₉S₈-Catalyzed growth of thin-walled graphite microtubes for robust, efficient overall water splitting, Chemsuschem 11 (2018) 4150–4155.

[37] B. Chen, X. He, F. Yin, H. Wang, D. Liu, R. Shi, J. Chen, H. Yin, MO-Co@N-doped carbon (M = Zn or Co): Vital roles of inactive Zn and highly efficient activity toward oxygen reduction/evolution reactions for rechargeable Zn-air battery, Adv. Funct. Mater. 27 (2017) 1700795.

[38] Z. Yu, N. Ji, J. Xiong, X. Li, R. Zhang, L. Zhang, X. Lu, Ruthenium-nanoparticle-loaded hollow carbon spheres as nanoreactors for hydrogenation of levulinic acid: Explicitly recognizing the void-confinement effect, Angew. Chem. Int. Ed. 60 (2021) 20786–20794.

[39] L. Yan, H. Wang, J. Shen, J. Ning, Y. Zhong, Y. Hu, Formation of mesoporous Co/CoSₓ/Metal-N-C@S, N-codoped hairy carbon polyhedrons as an efficient trifunctional electrocatalyst for Zn-air batteries and water splitting, Chem. Eng. J. 403 (2021) 126385.

[40] H. Li, Y. Liu, L. Huang, C. Jin, T. Zhang, P. Liu, L. Chen, W. Guo, T. Gu, G. Wang, 2D Metal-organic framework derived Co/CoSe₂ heterojunctions with interfacial electron redistribution as bifunctional electrocatalysts for urea-assisted rechargeable Zn–air batteries, J. Mater. Chem. A 11 (2023) 5179–5187.

[41] J. Gao, Y. Wang, H. Wu, X. Liu, L. Wang, Q. Yu, A. Li, H. Wang, C. Song, Z. Gao, M. Peng, M. Zhang, N. Ma, J. Wang, W. Zhou, G. Wang, Z. Yin, D. Ma, Construction of a sp³/sp² carbon interface in 3D N-doped nanocarbons for the oxygen reduction reaction, Angew. Chem. Int. Ed. 58 (2019) 15089–15097.

[42] Z. Lu, B. Wang, Y. Hu, W. Liu, Y. Zhao, R. Yang, Z. Li, J. Luo, B. Chi, Z. Jiang, M. Li, S. Mu, S. Liao, J. Zhang, X. Sun, An isolated zinc-cobalt atomic pair for highly active and durable oxygen reduction, Angew. Chem. Int. Ed. 58 (2019) 2622–2626.

[43] T. Sun, F. Huang, J. Liu, H. Yu, X. Feng, X. Feng, Y. Yang, H. Shu, F. Zhang, Strengthened d-p orbital-hybridization of single atoms with sulfur species induced bidirectional catalysis for lithium-sulfur batteries, Adv. Funct. Mater. 33 (2023) 2306049.

[44] W. Liu, H. Zhang, W. Ye, B. Xiao, Z. Sun, Y. Cheng, M.S. Wang, Regulating the wettability of hard carbon through open mesochannels for enhanced K⁺ storage, Small 19 (2023) 2300605.

[45] J. Kang, G. Liu, Q. Hu, Y. Huang, L.M. Liu, L. Dong, G. Teobaldi, L. Guo, Parallel nanosheet arrays for industrial oxygen production, J. Am. Chem. Soc. 145 (2023) 25143–25149.

[46] S. Zhao, T. Liu, Y. Dai, J. Wang, Y. Wang, Z. Guo, J. Yu, I.T. Bello, M. Ni, Pt/C as a bifunctional ORR/iodide oxidation reaction (IOR) catalyst for Zn-air batteries with unprecedentedly high energy efficiency of 76.5%, Appl. Catal. B: Environ. 320 (2023) 121992.

[47] K. Tang, H. Hu, Y. Xiong, L. Chen, J. Zhang, C. Yuan, M. Wu, Hydrophobization engineering of the air-cathode catalyst for improved oxygen diffusion towards efficient zinc-air batteries, Angew. Chem. Int. Ed. 61 (2022) 202202671.

[48] Y. Huang, J. Jiang, B. Shi, K. Ryan, J. Wang, Highly efficient oxygen evolution reaction enabled by phosphorus doping of the Fe electronic structure in iron-nickel selenide nanosheets, Adv. Sci. 8 (2021) 2101775.

[49] S.S. Jeon, P.W. Kang, M. Klingenhof, H.Y.J. Lee, F. Dionigi, P. Strasser, Active surface area and intrinsic catalytic oxygen evolution reactivity of NiFe LDH at reactive electrode potentials using capacitances, ACS Catal. 13 (2023) 1186–1196.

[50] M.M. Fan, Z.M. Wang, K. Sun, A. Wang, Y.Y. Zhao, Q.X. Yuan, R.B. Wang, J. Raj, J. Wu, J.C. Jiang, L. Wang, N-B-OH Site-activated graphene quantum dots for boosting electrochemical hydrogen peroxide production, Adv. Mater. 35 (2023) 2209086.

[51] J. Anjana, A. Muthukrishnan, Effect of local pH change on non-PGM catalysts – a potential-dependent mechanistic analysis of the oxygen reduction reaction, Catal. Sci. Technol. 12 (2022) 6246–6255.

[52] L. Yang, J. Shui, L. Du, Y. Shao, J. Liu, L. Dai, Z. Hu, Carbon-based metal-free ORR electrocatalysts for fuel cells: Past, present, and future, Adv. Mater. 31 (2019) 1804799.

[53] C. Yang, F. Sun, Z. Qu, X. Li, W. Zhou, J. Gao, Interfacial O₂ Accumulation affects microenvironment in carbon-based electrocatalysts for H₂O₂ production, ACS Energy Lett. 7 (2022) 4398–4407.

[54] H. Lei, L. Ma, Q. Wan, S. Tan, Z. Wang, W. Mai, Porous carbon nanofibers confined NiFe alloy nanoparticles as efficient bifunctional electrocatalysts for Zn-air batteries, Nano Energy 104 (2022) 107941.

[55] H. Yang, G. Li, G. Jiang, Z. Zhang, Z. Hao, Heterogeneous selective oxidation over supported metal catalysts: From nanoparticles to single atoms, Appl. Catal. B: Environ. 325 (2023) 122384.

[56] C. Weng, J. Ren, H. Wang, X. Lv, Y. Song, Y. Wang, L. Chen, W. Tian, Z. Yuan, Triple-phase oxygen electrocatalysis of hollow spherical structures for rechargeable Zn-air batteries, Appl. Catal. B: Environ. 307 (2022) 121190.

[57] X. Fu, G. Jiang, G. Wen, R. Gao, S. Li, M. Li, J. Zhu, Y. Zheng, Z. Li, Y. Hu, L. Yang, Z. Bai, A. Yu, Z. Chen, Densely accessible Fe-Nx active sites decorated mesoporous-carbon-spheres for oxygen reduction towards high performance aluminum-air flow batteries, Appl. Catal. B: Environ. 293 (2021) 120176.

[58] Y. He, Z. Zhao, Y. Cui, W. Shang, Y. Chen, P. Tan, Boosting gaseous oxygen transport in a Zn-air battery for high-rate charging by a bubble diode-inspired air electrode, Energy Storage Mater. 57 (2023) 360–370.

[59] W. Cai, J. Geng, S. Zhao, Y. Zhu, Y. Wang, Q. Chen, K. Guo, Simulation of OH⁻ and oxygen transport in the air-cathode catalyst layer of microbial fuel cells, Electrochem. Commun. 151 (2023) 107494.

[60] Y. Ma, D. Chen, W. Li, Y. Zheng, L. Wang, G. Shao, Q. Liu, W. Yang, Highly dispersive Co@N-C catalyst as freestanding bifunctional cathode for flexible and rechargeable zinc-air batteries, Energy Environ. Mater. 5 (2022) 543–554.

[61] W. Li, J. Wang, J. Chen, K. Chen, Z. Wen, A. Huang, Core-shell carbon-based bifunctional electrocatalysts derived from COF@MOF hybrid for advanced rechargeable Zn-air batteries, Small 18 (2022) 2202018.

[62] X. Yuan, J. Yin, Z. Liu, X. Wang, C. Dong, W. Dong, M.S. Riaz, Z. Zhang, M.Y. Chen, F. Huang, Charge-transfer-promoted high oxygen evolution activity of Co@Co₉S₈ core-shell nanochains, ACS Appl. Mater. Inter. 10 (2018) 11565–11571.

[63] S.K. Biswal, C. Ranjan, Suppressing H₂O₂ formation in the oxygen reduction reaction using Co-doped copper oxide electrodes, J. Mater. Chem. A 10 (2022) 22042–22057.

[64] T. Pauporté, L. Mendoza, M. Cassir, M.C. Bernard, J. Chivot, Direct low-temperature deposition of crystallized CoOOH films by potentiostatic electrolysis, J. Electrochem. Soc. 152 (2005) 49.

[65] M. Jiang, C. Fu, R. Cheng, W. Zhang, T. Liu, R. Wang, J. Zhang, B. Sun, Integrated and binder-free air cathodes of Co₃Fe₇ nanoalloy and Co₅.₄₇N encapsulated in nitrogen-doped carbon foam with superior oxygen reduction activity in flexible aluminum-air batteries, Adv. Sci. 7 (2020) 2000747.

[66] Z. Yu, N. Ji, J. Xiong, Y. Han, X. Li, R. Zhang, Y. Qiao, M. Zhang, X. Lu, Ultrafine ruthenium clusters shell-embedded hollow carbon spheres as nanoreactors for channel microenvironment-modulated furfural tandem hydrogenation, Small 18 (2022) 2201361.

[67] Y. Wang, T. Yang, X. Fan, Z. Bao, A. Tayal, H. Tan, M. Shi, Z. Liang, W. Zhang, H. Lin, R. Cao, Z. Huang, H. Zheng, Anchoring Fe species on the highly curved surface of S and N Co-doped carbonaceous nanosprings for oxygen electrocatalysis and a flexible Zinc-air battery, Angew. Chem. Int. Ed. 63 (2024) 202313034.

[68] X. Zhong, Z. Zheng, J. Xu, X. Xiao, C. Sun, M. Zhang, J. Ma, B. Xu, K. Yu, X. Zhang, H.M. Cheng, G. Zhou, Flexible zinc-air batteries with ampere-hour capacities and wide-temperature adaptabilities, Adv. Mater. 35 (2023) 2209980.

[69] W. Zhai, Y. He, Y.-e Duan, S. Guo, Y. Chen, Z. Dai, L. Liu, Q. Tan, Densely populated trimetallic single-atoms for durable low-temperature flexible zinc-air batteries, Appl. Catal. B: Environ. 342 (2024) 123438.